Vapor Growth of All-Inorganic 2D Ruddlesden–Popper Lead- and Tin-Based Perovskites

Xinting Shuai, Siraj Sidhik, Mingrui Xu, Xiang Zhang, Michael de Siena, Laurent Pedesseau, Hao Zhang, Guanhui Gao, Anand Puthirath, Wenbin Li, et al.

Vapor growth of all-inorganic 2D Ruddlesden-Popper lead- and tin-based perovskites

Xinting Shuai, Siraj Sidhik, Mingrui Xu, Xiang Zhang, Michael De Siena, Laurent Pedesseau, Hao Zhang, Guanhui Gao, Anand B. Puthirath, Wenbin Li, Ayush Agrawal, Jianan Xu, Jin Hou, Jessica H. Persaud, Jeremy Daum, Anamika Mishra, Yafei Wang, Robert Vajtai, Claudine Katan, Mercouri G. Kanatzidis, Jacky Even, Pulickel M. Ajayan and Aditya D. Mohite**

Author Information

Corresponding Authors

Pulickel M. Ajayan - *Department of Materials Science and NanoEngineering, Rice University, Houston, Texas, 77005, United States;* Email: ajayan@rice.edu

Aditya D. Mohite - *Department of Chemical and Biomolecular Engineering, Rice University, Houston, Texas, 77005, United States; Department of Materials Science and NanoEngineering, Rice University, Houston, Texas, 77005, United States;* Email: adm4@rice.edu

Authors

Xinting Shuai - *Department of Materials Science and NanoEngineering, Rice University, Houston, Texas, 77005, United States*

Siraj Sidhik - *Department of Materials Science and NanoEngineering, Rice University, Houston, Texas, 77005, United States*

Mingrui Xu - *Department of Materials Science and NanoEngineering, Rice University, Houston, Texas, 77005, United States*

Xiang Zhang - *Department of Materials Science and NanoEngineering, Rice University, Houston, Texas, 77005, United States*

Michael De Siena - *Department of Chemistry and Department of Materials Science and Engineering, Northwestern University, Evanston, Illinois, 60208, United States*

Laurent Pedesseau - *Univ Rennes, INSA Rennes, CNRS, Institut FOTON – UMR6082, Rennes F-35000, France*

Hao Zhang - *Department of Chemical and Biomolecular Engineering, Rice University, Houston, Texas, 77005, United States; Applied Physics Graduate Program, Smalley-Curl Institution, Houston, TX 77005, United States*

Guanhui Gao - *Department of Materials Science and NanoEngineering, Rice University, Houston, Texas, 77005, United States*

Anand B. Puthirath - *Department of Materials Science and NanoEngineering, Rice University, Houston, Texas, 77005, United States*
Wenbin Li - *Department of Chemical and Biomolecular Engineering, Rice University, Houston, Texas, 77005, United States; Applied Physics Graduate Program, Smalley-Curl Institution, Houston, TX 77005, United States*
Ayush Agrawal - *Department of Chemical and Biomolecular Engineering, Rice University, Houston, Texas, 77005, United States*
Jianan Xu - *Department of Materials Science and NanoEngineering, Rice University, Houston, Texas, 77005, United States*
Jin Hou - *Department of Materials Science and NanoEngineering, Rice University, Houston, Texas, 77005, United States*
Jessica H. Persaud - *Department of Chemical and Biomolecular Engineering, Rice University, Houston, Texas, 77005, United States*
Jeremy Daum - *Department of Materials Science and NanoEngineering, Rice University, Houston, Texas, 77005, United States*
Anamika Mishra - *Department of Chemical and Biomolecular Engineering, Rice University, Houston, Texas, 77005, United States*
Yafei Wang - *School of Mechanical and Electric Engineering, Guangzhou University, Guangzhou, Guangdong, 510006, China*
Robert Vajtai - *Department of Materials Science and NanoEngineering, Rice University, Houston, Texas, 77005, United States*
Claudine Katan - *Univ Rennes, ENSCR, INSA Rennes, CNRS, ISCR -UMR6226, Rennes F-35000, France*
Mercouri G. Kanatzidis - *Department of Chemistry and Department of Materials Science and Engineering, Northwestern University, Evanston, Illinois, 60208, United States*
Jacky Even - *Univ Rennes, INSA Rennes, CNRS, Institut FOTON – UMR6082, Rennes F-35000, France*

Abstract: The 2D Ruddlesden-Popper (RP) perovskites $Cs_2PbI_2Cl_2$ (with Pb-based n=1) and $Cs_2SnI_2Cl_2$ (with Sn-based n=1) stand out as unique and rare instances of entirely inorganic constituents within the more expansive category of organic/inorganic 2D perovskites. These materials have recently garnered significant attention for their strong UV-light responsiveness, exceptional thermal stability, and theoretically predicted ultrahigh carrier mobility. In this study, we synthesized Pb and Sn-based n=1 2D RP perovskite films covering millimeter-scale areas for the first time, utilizing a one-step chemical vapor deposition (CVD) method under atmospheric conditions. These films feature perovskite layers oriented horizontally relative to the substrate. Multilayered $Cs_3Pb_2I_3Cl_4$ (Pb-based n=2) and $Cs_3Sn_2I_3Cl_4$ (Sn-based n=2) films were also obtained for the first time, and their crystallographic structures were refined by combining X-ray diffraction (XRD) and density functional theory (DFT) calculations. DFT calculations and experimental optical spectroscopy support band gap energy shifts related to the perovskite layer thickness. We demonstrate bias-free photodetectors using the Sn-based n=1 perovskite with reproducible photocurrent and a fast 84 ms response time. The present work not only demonstrates the growth of high-quality of all-inorganic multilayered 2D perovskites by the CVD method but also suggests their potential as promising candidates for future optoelectronic applications.

Keywords: all-inorganic perovskites, 2D perovskites, tin-based perovskites, CVD, photodetector

Two-dimensional (2D) $A'_2A_{n-1}B_nX_{3n+1}$ hybrid Ruddlesden-popper (RP) perovskites, where A' is a large organic cation located in the interlayers, A is a cation in the perovskite layers, B is a divalent metal and X is a halogen atom, are solution-processed quantum well superlattices, n is the number of vertically stacked perovskite BX_6 octahedra in the quantum well. These 2D hybrid RP halide perovskites have attracted more attention these years owing to their tunable optical and electronic properties and excellent stability.[1,2] They have also been widely explored in the framework of light emitting diodes (LED), field-effect transistors (FET) , photodetectors, and solar cells etc.[3,4]

Differing from traditional organic-inorganic hybrid 2D RP perovskites introduced above, all-inorganic 2D RP perovskites use smaller inorganic cations, such as Cs^+ and Rb^+, instead of large organic interlayer spacers.[5] Because of this, all-inorganic perovskites are expected to exhibit

greater robustness under extreme conditions and improved optoelectronic properties.[6] In 2018, Kanatzidis and co-workers were the first to report the existence of all-inorganic 2D RP phase halide perovskite single crystals of $Cs_2PbI_2Cl_2$ and $Cs_2SnI_2Cl_2$ with n=1 using a melt growth approach which demonstrated a direct band gap with small carrier effective masses, strong UV-light response, and remarkable ambient and thermal stability.[5,7] Following this work, ultrahigh carrier mobilities, were predicted for these structures by Liu et al., based on density functional theory (DFT) calculations.[6] In addition, the enhanced photocurrent after inducing pressure and intrinsically ultralow thermal conductivity of the $Cs_2PbI_2Cl_2$ perovskites were further analyzed.[8,9] These novel fully inorganic 2D RP compounds pose as promising candidates for high-performance optoelectronic devices.

Most of the Pb-based n=1 and Sn-based n=1 perovskites have been synthesized using solid-state processes and the Bridgman method.[5,7,8,9] In addition to these processes, it has been shown that 2D $Cs_2PbI_2Cl_2$ nanosheets and nanoplates can be fabricated by solution methods.[10,11] However, to the best of our knowledge, growing inorganic 2D RP perovskites by chemical vapor deposition (CVD) has not yet been explored. CVD is a common, solution-free fabrication method for semiconductor materials, such as MoS_2,[12,13] Graphene, and h-BN,[14,15] and is well known for its ability to produce highly crystalline, stable films with low surface defects and controlled morphology at a low cost.[16] In recent years, CVD has been shown to successfully achieve different morphologies of 3D perovskites, such as $CsPbX_3$(X=Br, Cl or I) nanoplates and nanowires.[17-18] Meanwhile, vapor-based techniques have also garnered significant attention as pivotal technologies in perovskite solar cell fabrication,[19,20] as well as in the production of perovskite/silicon tandem solar cells,[21,22] and the essential implementation of evaporation processes for surface passivation layers.[23,24]

Here we report for the first time all-inorganic RP 2D Pb and Sn-based n=1 and n=2 film with millimeter size that were grown on different substrates by a one-step CVD method under atmospheric pressure. Using transmission electron microscopy (TEM), XRD, energy dispersive x-ray analysis (EDAX), and grazing incident wide angle x-ray spectroscopy (GIWAXS), we were able to confirm the horizontal orientation of the stacking axis with respect to the substrate and atomic ratios in lead and tin based perovskites n=1 and n=2 materials. The binding energies of Pb^{2+} and Sn^{2+} measured via x-ray photoelectron spectroscopy (XPS) are consistent with the

expected electronic structures of layered perovskites. Using photoluminescence (PL) and absorbance, we measured optical band gaps of 2.99 eV, 2.95 eV for $Cs_2PbI_2Cl_2$ (n=1) and $Cs_3Pb_2I_3Cl_4$ (n=2), respectively, and $Cs_2SnI_2Cl_2$ (n=1) and 2.54 eV, 2.43 eV for $Cs_3Sn_2I_3Cl_4$ (n=2) , respectively. These values are consistent with electronic band gap obtained from DFT band structure calculation. We also constructed a lead-free photodetector using a 2D tin-based n=1 film, demonstrating enhanced photocurrent upon light exposure. Additionally, we observed a bias-free, reproducible photocurrent response during ON/OFF cycles, achieving a rapid response time of 84ms for tin-based perovskite photodetector.

Results and Discussion

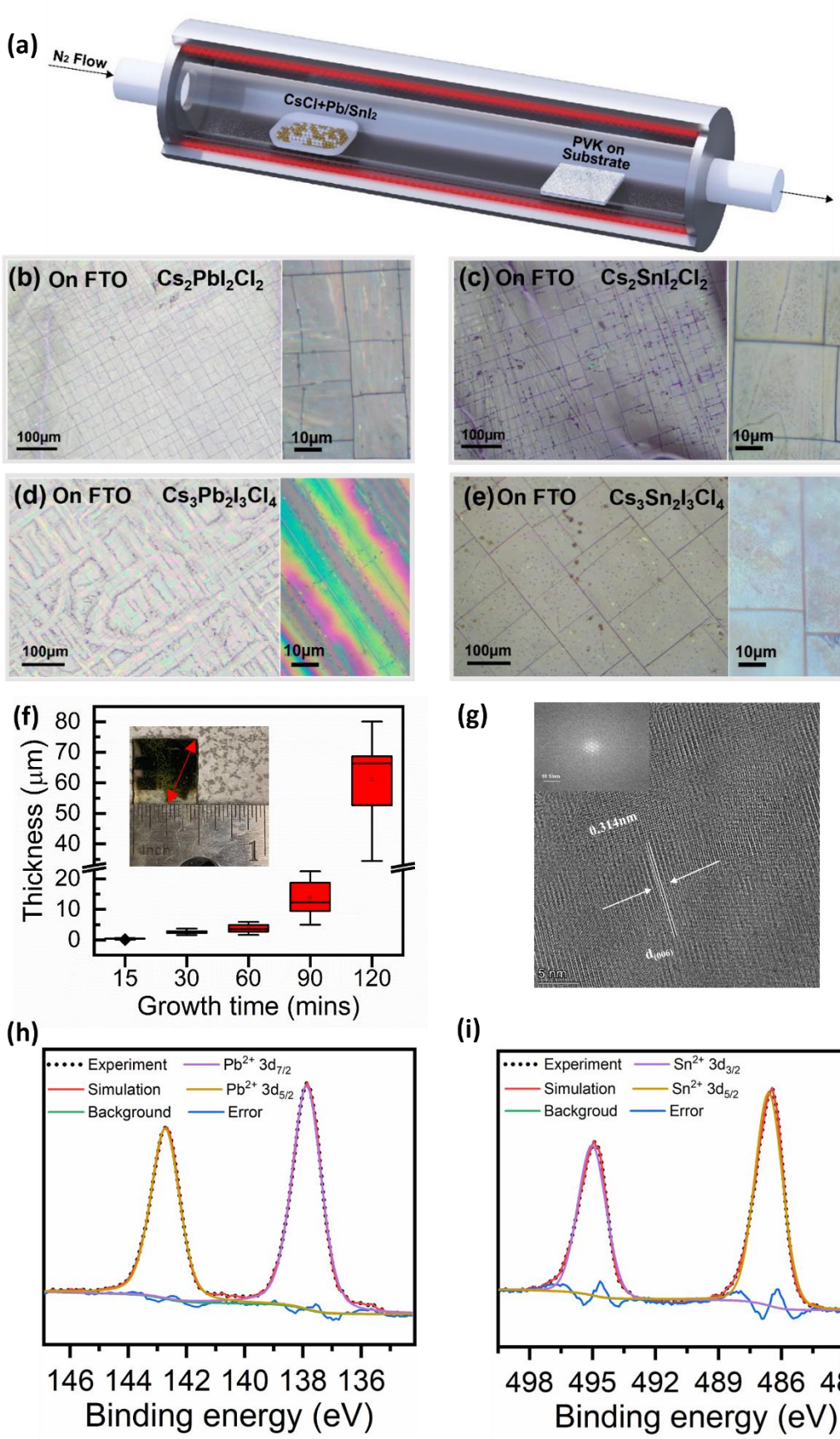
(a)
N2 Flow
CsCl+Pb/SnI2
PVK on Substrate
(b) On FTO Cs2PbI2Cl2
100μm
10μm
(c) On FTO Cs2SnI2Cl2
100μm
10μm
(d) On FTO Cs3Pb2I3Cl4
100μm
10μm
(e) On FTO Cs3Sn2I3Cl4
100μm
10μm
(f)
Thickness (μm)
0
10
20
40
50
60
70
80
15
30
60
90
120
Growth time (mins)
(g)
0.314nm
5 nm
(h)
Experiment
Simulation
Background
Pb2+ 3d7/2
Pb2+ 3d5/2
Error
146 144 142 140 138 136
Binding energy (eV)
(i)
Experiment
Simulation
Backgroud
Sn2+ 3d3/2
Sn2+ 3d5/2
Error
498 495 492 489 486 483
Binding energy (eV)

Figure 1. | Physical Properties of Perovskite (PVK) films. (a) Schematic diagram shows the fabrication of 2D perovskite films by vaporizing CsCl and Pb/SnI_2 precursors and depositing on different substrates with one-step CVD method under atmospheric pressure. Optical microscopy images of films of (b) Pb-based n=1, (c) Sn-based n=1, (d) Pb-based n=2, (e) Sn-based n=2 grown on Fluorine Tin Oxide (FTO). (f) Film thickness of Sn-based n=1 for different growth times (Inset image is the film size photo of Sn-based n=1 when growth time is 15 min). (g) High resolution TEM (HRTEM) images and Fast Fourier transform (FFT) patterns (inserts) of Pb-based n=1 film. XPS spectra of (h) Pb^{2+} from Pb-based n=1and (i) Sn^{2+} from Sn-based n=1.

Pb and Sn-based n=1 2D perovskite films were grown in a one-zone atmosphere pressure CVD furnace. Cesium chloride (CsCl) was mixed with lead iodide (PbI_2) and tin iodide (SnI_2) powders in stoichiometric ratios for n=1 and placed upstream to produce Pb and Sn-based n=1 2D perovskite, respectively (Figure 1a). FTO, Nickel Oxide (NiO), c-plane sapphire, and SiO_2 were placed downstream as substrates. Mixed precursors were vaporized between 600 °C and 650 °C with 80 standard cubic centimeters per minute (sccm) high-purity Nitrogen (N_2) as a carrier gas. The distance between the substrate and the furnace thermal block is used to mark the specific position and the temperature gradient of substrates. More details about growth optimization can be found in the experimental section.

Several substrates were studied for large area, continuous 2D perovskite films deposition. For Pb-based n=1 2D perovskites, films were not only epitaxially grown on oriented c-plane sapphire substrates (Figure S1a, Supporting Information) but also on amorphous substrates such as FTO, NiO and SiO_2 substrates (Figure 1b and Figure S1b, c, Supporting Information). However, Sn-based n=1 2D perovskites can be only grown on FTO and NiO amorphous substrates (Figure 1c and Figure S1d, Supporting Information). Films with millimeter size and “tiled” angular-shaped morphology can be obtained on each of the substrates. With excess $PbCl_2$ or $SnCl_2$ in precursors and changing the stoichiometry of mixed powders, large areas of pure Pb or Sn-based n=2 2D perovskite films could be synthesized with the same “tiled” angular shape morphology as n=1 in Figure 1d and e. These Pb and Sn-based n=2 films can also be grown on the same substrates as their respective n=1.

Different growth temperatures and deposition times were investigated to elucidate the morphology of Sn-based n=1 perovskite observed in Figure S1e, Supporting Information. At a growth temperature of 600°C, we observed small areas of large crystals with size of 20-30 μm and numerous tiny particles with size less than 10 μm distributed on the substrate. Upon increasing the temperature to 650°C, crystal growth started and the smaller crystallites dissolved while large crystals grew and partially connected, ultimately merging into a continuous film with increasing deposition time. The mechanism of this 2D perovskite formation involved the merging of large crystallites at the expense of precursor small particles, as confirmed by the disappearance of SnI_2 peak in Figure S1f, Supporting information. This crystallization phenomenon exhibited behavior consistent with the Ostwald ripening approach,[25] which is well-known as the thermodynamically driven kinetics for perovskite growth.[26,27] It should be noticed that the formation of "tiled" angular-shaped morphology occurred when the temperature was initially raised to 650°C (Figure S1g, Supporting information).

The thickness of 2D perovskite films usually range from a few nm to almost 80 μm depending on growth time and, remarkably, we were able to obtain lateral sizes of a few mm using only a 15 min growth period. A profilometer was used to measure the thicknesses of Sn-based n=1 2D perovskite films as a function of the growth time ranging from 15 min to 120 min. Figure 1f reveals that the mean thickness of the Sn-based n=1 2D perovskite film slowly increases from 0.42 μm to 2.6 μm over 15, 30, and 60 min growth times, before abruptly jumping to 13.8 μm and 61.0 μm for 90 and 120 min growth times, respectively. Notably, the maximum thickness of 80.0 μm was achieved with a growth time of 120 min, which is considerably thicker than previously reported perovskites grown via CVD. The inset image in Figure 1f shows a photograph of a Sn-based n=1 2D perovskite film for a growth time of 15 min, the lateral size of the film reached 9.3 mm, effectively covering nearly the entire area of the FTO substrate electrode. These results demonstrate the exceptional growth capability of the CVD method in producing high-quality perovskite films with precise thickness control.

To measure the inter reticular distance of 2D perovskites at the atomic level, TEM images were taken from samples transferred onto the TEM grid by solution method. From Figure 1g and Figure S2a in the Supporting information, it is evident that the Pb-based n=1 2D perovskites formed layered crystals with a measured inter reticular distance of 0.314 nm using high-resolution

transmission electron microscopy (HRTEM), as depicted in Figure 1g. This distance corresponds to the dominate (006) plane, as confirmed by XRD results. Additionally, the inserted fast Fourier transform (FFT) pattern indicates a tetragonal crystal structure for the lead-based perovskite. Furthermore, high angle annular dark field (HAADF)-scanning transmission electron microscopy (STEM)-energy dispersive spectrometry (EDS) mapping images demonstrated a uniform distribution of Cs, Pb, I, and Cl elements throughout the crystal, as shown in Figure S2b-f in the supplementary information.

Pb and Sn-based n=1 2D perovskite films were exposed to ambient conditions for 3 hours to access their initial stability. From x-ray photoelectron spectroscopy (XPS) measurements, we can only see the binding energies relating to Pb^{2+} $3d_{7/2}$ and Pb^{2+} $3d_{5/2}$ at 137.9 eV and 142.8 eV in Figure 1h. Peaks relating to Sn^{2+} $3d_{5/2}$ and Sn^{2+} $3d_{3/2}$ binding energy at 486.6 eV and 495 eV, as seen in Figure 1i, match the spectra. The absence of Sn^{4+} ions, a product of fast degradation of Sn-based perovskites caused by p-type defects in its electronic structure,[28] proves the stability of Sn-based n=1 2D perovskite film.

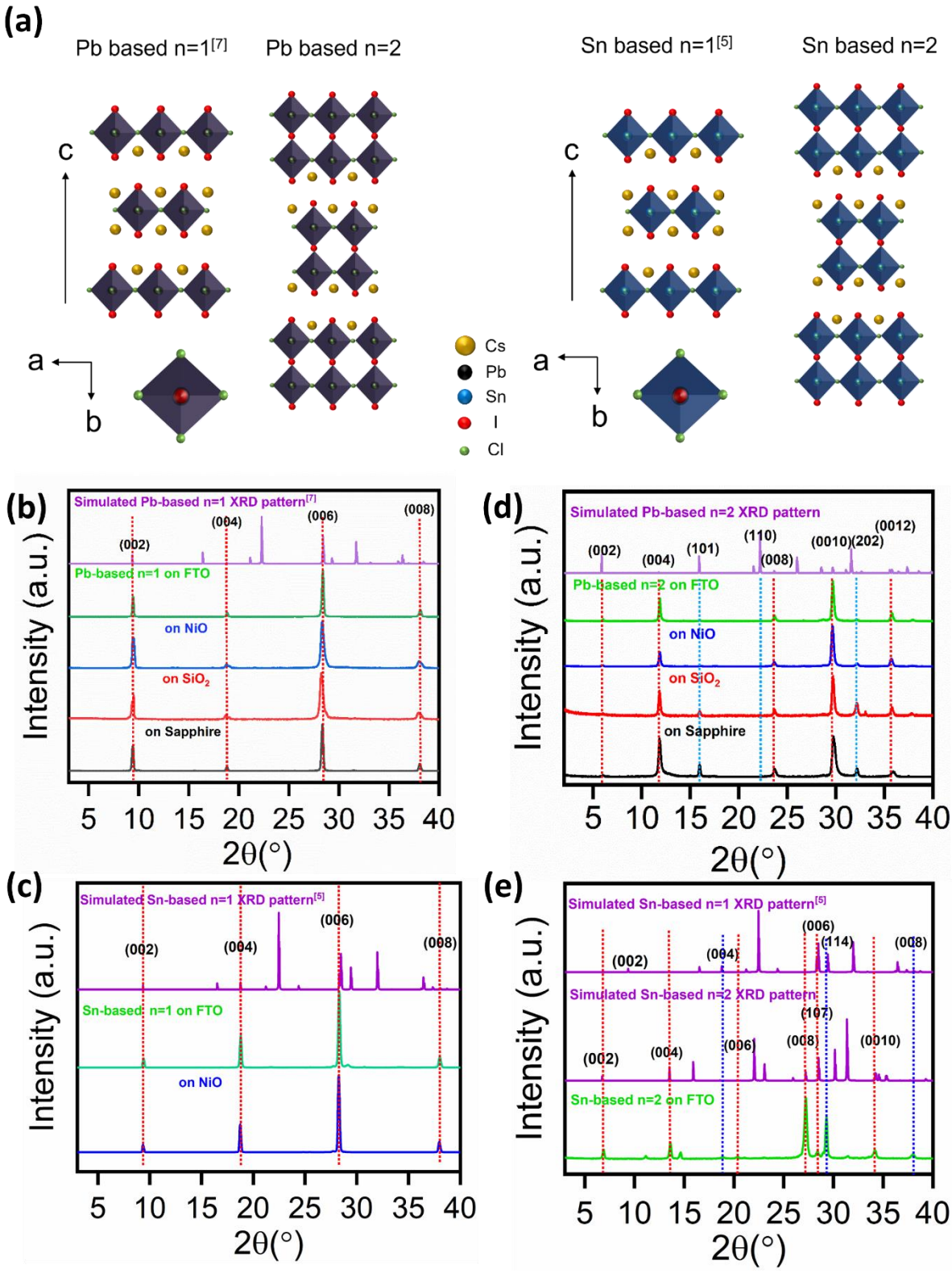

Figure 2. | Structural information of 2D Perovskite films. (a) Crystal structures of Pb and Sn-based n=1 and n=2 from side view and top-down view, crystallographic structures of n=2 were proposed

from a combined experimental/theoretical analysis. Experimental XRD patterns of Pb-based (b) n=1 and (d) n=2 films on FTO, NiO, SiO_2, and sapphire substrates. The computed diffraction patterns (purple color) of Pb-based n=1[7] and n=2 refined from DFT calculations were added. Experimental XRD patterns of Sn-based (c) n=1 on FTO and NiO substrates and (e) n=2 films on FTO substrate. The computed diffraction patterns (purple color) of Sn-based n=1[5] and n=2 refined from DFT calculation are included.

Both 2D Pb and Sn-based n=1 perovskites have K_2NiF_4-type structure[29] and belong to tetragonal space group *I*4/*mmm* with the unit cell parameters for Pb-based n=1 of a = b = 5.6385(8) Å, c = 18.879(4) Å and for Sn-based n=1 of a = b = 5.5905(3) Å, c = 18.8982(13) Å.[7,5] The 2D layer plane consists of corner-sharing $[BI_2Cl_2]^{4-}$ octahedra, where I ions occupy out-of-plane sites and Cl ions occupy in-plane sites (Figure 2a). Slices containing one and two octahedra-thick layers represent the n=1 and n=2 structures, whereas Cs ions act as the spacers and provide charge balancing. Here, Pb and Sn-based n=1 perovskites have a standard single-layer RP structure and Pb and Sn-based n=2 possess a standard bilayer RP structure.

Figure 2b shows XRD patterns of as-grown Pb-based n=1 2D perovskite films on FTO, NiO, SiO_2 and c-plane sapphire substrates. All films grown on these substrates showed similar peaks at 9.56°, 18.78°, 28.4° and 38.05°, which align with the (002), (004), (006) and (008) planes of simulated Pb-based n=1 powder XRD.[7] For Sn-based n=1 2D perovskite films grown on FTO and NiO substrates, XRD patterns (Figure 2c) exhibit similar peaks at 9.41°, 18.77°, 28.3° and 38.02°, further corresponding to the (002), (004), (006) and (008) planes respectively of simulated Sn-based n=1 powder XRD data.[5] After increasing the $[PbI_2Cl_4]^{4-}$ octahedral units introduced to the RP structure, perovskite single-layers were transformed into bilayers due to unit cell expansion, which resulted in an increase of unit cell along the c stacking axis with a and b parameters nearly unchanged (Table 1), as well as an additional low angle peak resulting from increased spacing distance, as shown in the XRD pattern in Figure 2d.[30]

By adjusting the ratio of precursors evaporated, low angle peaks at 5.93° and 6.75° were measured in Pb and Sn-based n=2 2D perovskite films, respectively (Figure 2d,e), corresponding to the spacing distance of 1.49 nm and 1.31 nm. This shows the existence of n=2 RP all-inorganic perovskites. Peaks at 11.8°, 23.67°, 29.74° and 35.87° belong to the second, fourth, fifth and sixth order of the low angle peak for Pb-based n=2 perovskites. The principle is the same for peaks at

13.51°, 27.1°, 33.8° for Sn-based n=2 perovskites. These n=2 2D perovskite films show the same XRD peak positions on FTO, NiO, SiO_2 and c-plane sapphire substrates for Pb-based n=2 and FTO substrates for Sn-based n=2 perovskites. The simulated powder diffraction patterns for both Pb and Sn-based n=1 and n=2 are shown in Figure S3a-d, Supporting Information. We noted the presence of non-Sn-based n=2 related peaks in Fig. 2e, likely due to the degradation and oxidation of Sn-based perovskites during diffraction measurements under ambient conditions. Since this is the first discovery of the Sn-based n=2 phase, further research is needed to improve stability and understand the crystal structure in greater detail.

Table 1. Atomic ratios of Pb, Sn-based n=1 and n=2 films detected through EDAX-SEM measurement and unit cell parameters for Pb, Sn-based n=1[5,7] and n=2 extracted from powder diffraction patterns.

Compound	Cs	Pb	I	Cl	a(Å)	b(Å)	c(Å)
$Cs_2PbI_2Cl_2$ (n=1)	2.09	1	1.93	2.37	5.638	5.638	18.879
$Cs_3Pb_2I_3Cl_4$ (n=2)	3.22	2	3.36	4.2	5.655	5.655	30.100
$Cs_2SnI_2Cl_2$ (n=1)	2.03	1	2.09	2.05	5.590	5.590	18.898
$Cs_3Sn_2I_3Cl_4$ (n=2)	3.24	2	3.36	4.6	5.700	5.700	26.200

Atomic ratios of different n-values reported in Table 1 were averaged from data of several EDAX-SEM measurements (see Figure S4a-d as the example of EDAX-SEM measurement, Supporting Information). They are consistent with the stoichiometry as derived from the general inorganic RP chemical formula. The similarity between computed and measured atomic ratios is a good indication for the formation of these n=1 and n=2 2D perovskites. It's noteworthy that the proportion of Cl in the Sn-based n=2 is a bit larger than in the Pb-based n=2 compound. The fact that both n=1 compounds exhibit the same lattice parameter along the stacking is associated to that only Pb-I and Sn-I bonds are present along this axis for these compounds. The smaller c parameter

value observed in the Sn-based n=2 compound indicates that some Sn-I bonds are replaced by Sn-Cl ones.

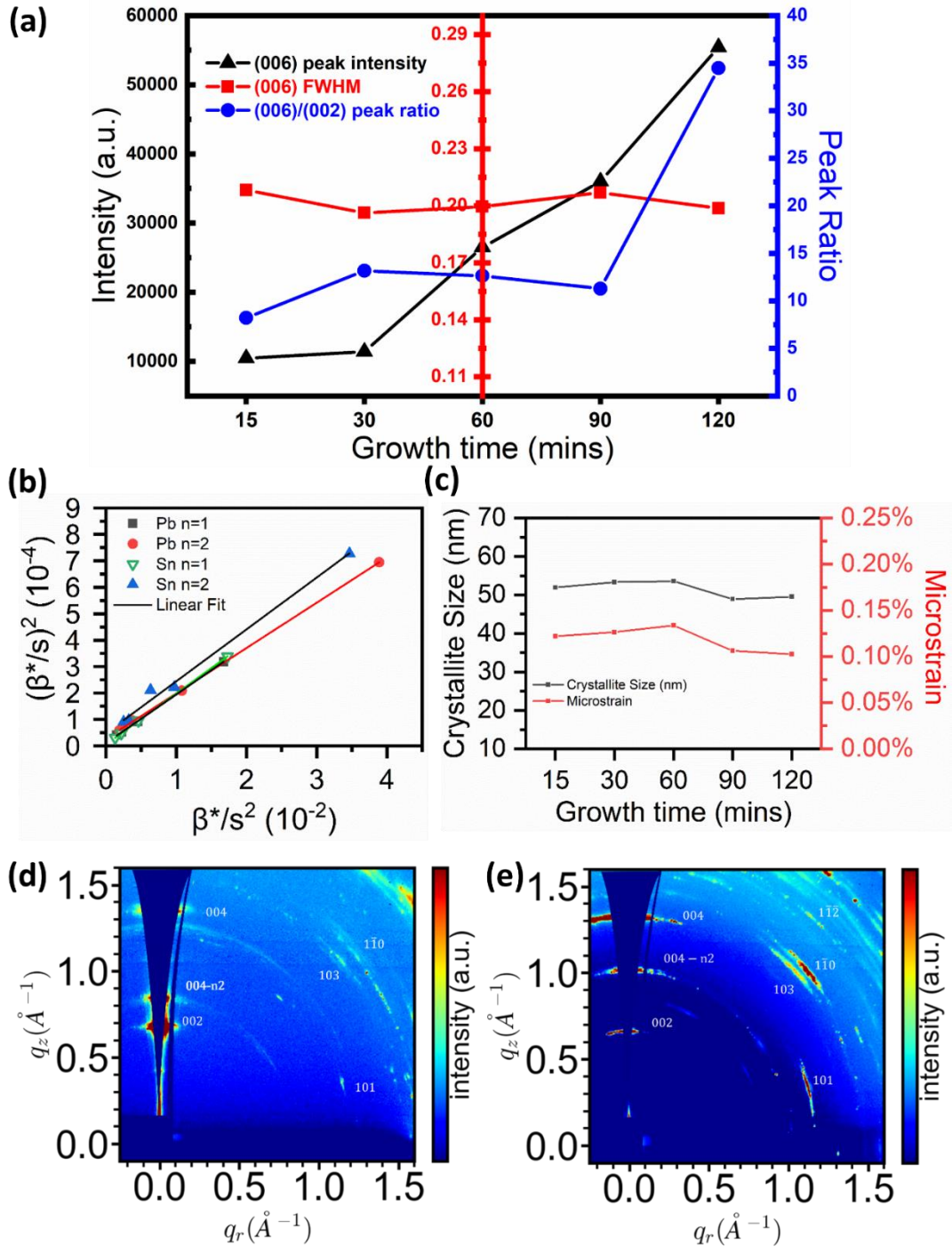

Figure 3. | Crystallite analysis of Pb and Sn-based 2D perovskite films. (a) (006) peak intensity (black), FWHM (red), (006)/ (002) peak ratio (blue) of Sn-based n=1 films for different deposition times. (b) Halder-Wagner plots for Pb and Sn-based n=1 and n=2 on FTO under 15 min growth time. (c) Sn-based n=1 film crystallite size (black) and microstrain (red) as a function of the growth time. GIWAXS patterns for (d) Pb-based n=1 and (e) Sn-based n=1 films.

We further examined the quality of the Sn-based n=1 films from the (006) peak intensity, (006)/ (002) peak ratio, and the corresponding FWHM of the (006) peak as a function of different CVD deposition time. According to Figure 3a, the (006) peak intensity increases continuously with longer deposition times, which is consistent with the increased thickness in Figure 1f. Additionally, we found that the (006)/(002) peak ratio remains unchanged for the first 90 min of growth. After the first 90 min, the intensity of (006) diffraction plane increases and becomes more prominent than the intensity of the (002) diffraction plane, suggesting a rapid development of (006) texture.[31] Furthermore, the FWHM extracted from (006) plane changes from 0.196° to 0.208° through different growth times. This small shift indicates a negligible change in the crystallinity for up to two hours of growth.

To explore the detailed crystal morphology of the Pb and Sn-based n=1 and n=2 films along out-of-plane orientations, we analyzed the crystallite size and strain distribution using Halder-Wagner[32,33] equations (1) (2) and (3), where θ is the position of Bragg peak, *K* is Scherrer constant (0.9), λ is the x-ray wavelength (1.0589Å), and $\beta(S)$ is the diffraction peak integral breadth tuned by variable *S*.

$$S = \frac{2Sin\theta}{\lambda} \quad (1)$$

$$\beta(S) = \beta(2\theta)\frac{cos\theta}{\lambda} \quad (2)$$

$$\left(\frac{\beta(s)}{S}\right)^2 = 4\varepsilon^2 + \frac{K}{L}\frac{\beta(s)}{S^2} \quad (3)$$

$$L = \frac{K\lambda}{\beta_L(2\theta)cos\theta} \quad (4)$$

$$\varepsilon = \frac{1}{4}\beta_\varepsilon(2\theta)\cot an\theta \quad (5)$$

The crystallite size lengths, L, and the micro-strains, ε, are calculated from the slope and intercept, y, of the linear fits of the Halder-Wagner plots. Therefore, the crystallite size L and the microstrain ε are extracted from the linear fitting of $(\beta(s)/S)^2$ as a function of $\beta(s)/S^2$ (Equation (4) and (5)). Halder-Wagner plots from these calculations, would provide more precise results for various microstructural parameters by analyzing the XRD peak broadening samples.[34] From Figure 3b, for Pb-based n=1 (black), n=2 (red), Sn-based n=1 (green), n=2 (blue) samples, L is calculated from the fitted slope to be ~ 49 nm, 52 nm, 52 nm and 51 nm, respectively, and ε is calculated from the y intercept to be ~ 0.16%, 0.26%, 0.12% and 0.34%, respectively. In addition, crystallite size and microstrain components were also analyzed as a function of Sn-based n=1 CVD growth time in Figure 3c, where both crystallite size and microstrain remain rather constant. The linear fitting comparison of crystallite analysis for Sn-based n=1 on FTO between 15 and 120 min growth time using Halder-Wagner plots in Figure S5, see Supporting Information, also confirmed the similar crystallite size and microstrain, indicating the crystalline quality is negligibly affected by the CVD growth time.

Next, we used GIWAXS to gain further insights into the crystal structure of Pb and Sn-based n=1 films. In Figure 3d, diffraction peaks of (002), (004), (103), (101) and (1 -1 0) appear as spots located at the scattering vector q= 0.67, 1.33, 1.5, 1.16 and 1.58 $Å^{-1}$, respectively, which corresponds to spacing distances of 0.94, 0.47, 0.42, 0.54, and 0.40 nm. Patterns in Figure 3e also show Sn-based n=1 diffraction spots of (002), (004), (103), (101), (1 -1 0), and (1 -1 -2) with q=0.66, 1.33, 1.5, 1.17, and 1.72 $Å^{-1}$ and spacing distance of 0.94, 0.47, 0.42, 0.54, 0.40, and 0.36 nm. We observed (004) n=2 peak from Figures 3d and 3e that might be surface localized defect states created from the surface selective grazing incidence X-Ray measurement.[35] The peak analysis from above is consistent with our XRD results and provides evidence of an oriented crystal structure.

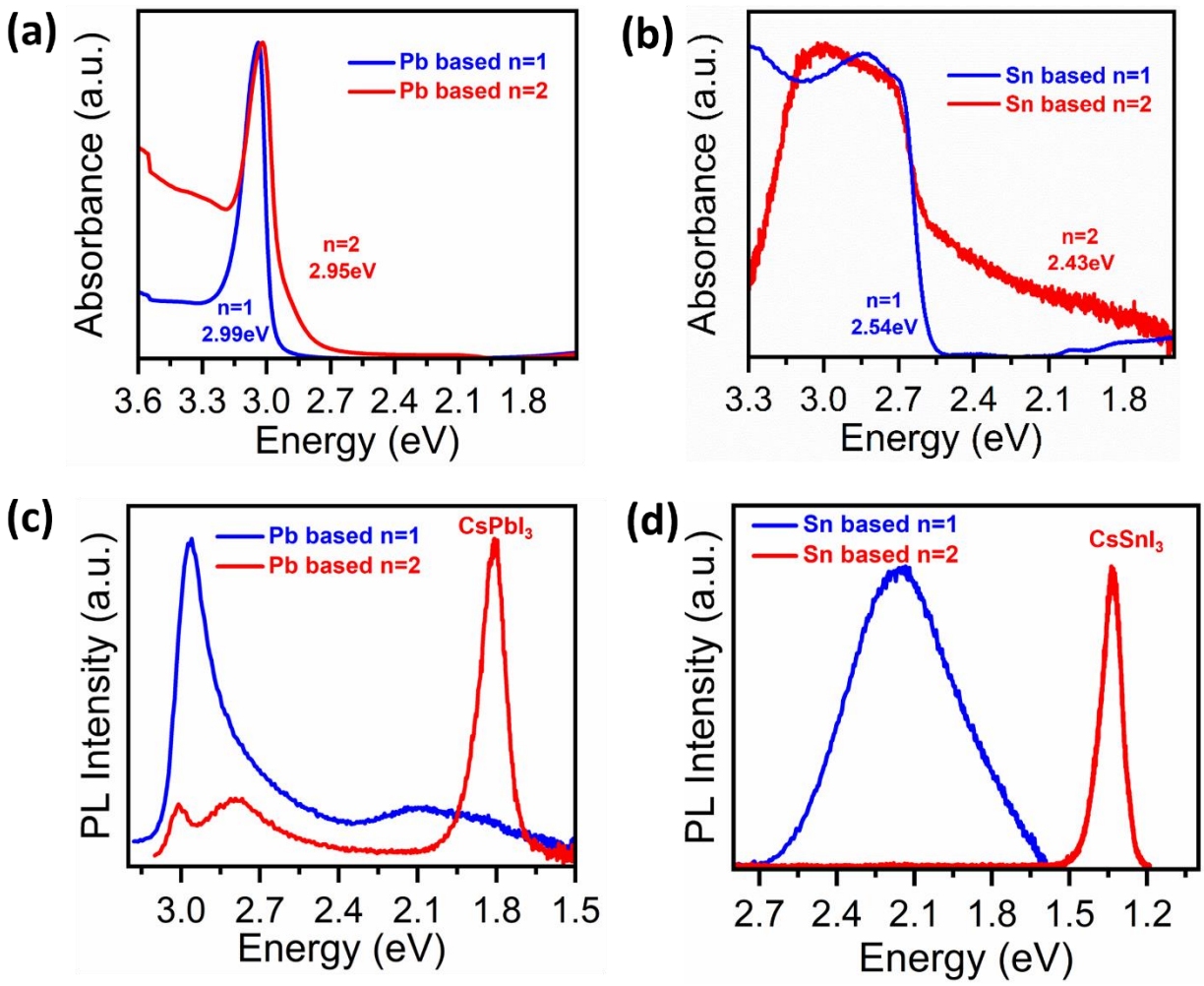

Figure 4. | Optical characterizations for Pb and Sn-based 2D perovskites**.** Optical absorbance of (a) Pb-based n=1 and n=2 perovskites (b) Sn-based n=1 and n=2 perovskites (Extracted optical band gap values are 2.99, 2.95 eV for Pb-based n=1 and n=2 and 2.54, 2.43 eV for Sn-based n=1 and n=2, respectively). PL spectra of (c) Pb-based n=1 and n=2 perovskites and (d) Sn-based n=1 and n=2 perovskites (excited at 365 nm with 150W Xe lamp).

Room-temperature absorbance and PL spectroscopy were used to investigate the optical properties of Pb and Sn-based n=1 and n=2 films. Absorbance was collected in transmission geometry and the optical band gaps were estimated by Tauc plot (details were discussed in experimental section). Sharp absorption edges with excitonic peaks for Pb-based n=1 and n=2 perovskites can be seen at

2.99 eV and 2.95 eV separately (extracted from Tauc plots in Figure S6a and Figure S6b, Supporting Information), as shown in Figure 4a. The estimated absorption edge for Pb-based n=1 is slightly smaller (by -50 meV) than reported previously in the literature for bulk grown crystals (3.04 eV).[7] For the Pb-based n=2 perovskite, a small red-shift of the absorption edge excitonic peak was detected when compared to n=1 and this is attributed to the fact that the Cl/I ratio in the n=2 structure is higher than in the n=1 structure at 4:3 and 1:1 respectively. It is well known that higher fractions of more electronegative Cl atoms in the perovskite structure widen the semiconducting band gap. This aspect is addressed in our supplementary information, where we discuss the results of our internal atomic DFT optimization. The optimization revealed significant distortions in the octahedra for the n=2 structures. Specifically, as shown in Figure S7, the observed distortion is an off-center distortion rather than a tilt distortion. This type of distortion further supports the small energy difference (~40 meV) between the excitonic peaks of the n=1 and n=2 Pb-based compounds. Therefore, while increasing the thickness of the RP layer from n=1 to n=2 decreases the band gap, the higher chlorine-to-iodine ratio and octahedral distortions compensate for the decrease by having an opposite effect. For Sn-based 2D perovskites, slightly more tunable optical band gaps for n=1 and n=2 could be deduced from the absorbance spectrum in Figure 4b, where sharp absorption edges from the excitonic peaks were estimated to be around 2.54 eV and 2.43 eV(extracted from Tauc plots in Figure S6c and Figure S6d, Supporting Information). For the structures for n=2 refined from DFT calculations, with numbers of assumptions including the stoichiometry and the space group (see Supporting Information), small decreases of the band gaps are predicted by comparison to n=1 compounds, in line with experimental trends.

The PL peak in Figure 4c for Pb-based n=1 at 2.96 eV closely matches the value of the optical absorption edge. A broad emission near the low-energy tail was also observed from 2.25 eV to 1.5 eV. Time-resolved photoluminescence (TRPL) was performed to explore the origin of this phenomenon, as illustrated in Figure S6e, Supporting Information. The t_1, t_2 and t_{avg} for Pb n=1 at 2.06 eV emission are 0.86, 7.7 and 4.3 ns, respectively, which are comparable with the carrier lifetimes reported in the literature.[7] These long carrier lifetimes and the presence of a broad emission with a large Stokes shift might be related to self-trapped excitons. For the Pb-based n=2

PL spectrum, three peaks located at 3.01 eV, 2.79 eV and 1.79 eV can be seen, which might be assigned to main exciton emission, to some state localized in the tail of the absorbance spectrum, and to a low energy emission that could be related to small $CsPbI_3$ domains, respectively.[36]

For Sn-based n=1, we also found a broad PL signal throughout the visible spectrum from 2.7 eV to 1.5 eV for Sn-based n=1 (Figure 4d). TRPL presented in Figure S6f, Supporting Information, reveals long carrier lifetimes (t_1) of 16.3 ns, for Sn n=1 emission at 2.16 eV. These long carrier lifetimes suggest that self-trapped excitons may underlie the broad PL emission in Sn-based perovskites. The Sn-based n=2 samples exhibit a sharp emission at 1.32 eV, consistent with the presence of a small amount of localized $CsSnI_3$ domains.[37] The limited quantity of $CsSnI_3$ may explain the absence of low-energy absorbance measurement. However, even in the presence of a small quantity of $CsSnI_3$, the PL spectrum exhibits low-energy state luminescence, likely resulting from energy funneling and subsequent recombination to the ground state.[38] It is important to note that significant ion migration is easily occurred in the in-plane direction of RP mixed halide perovskites,[39] particularly under laser irradiation.[40] That would be reasons for the superposition of several phases.

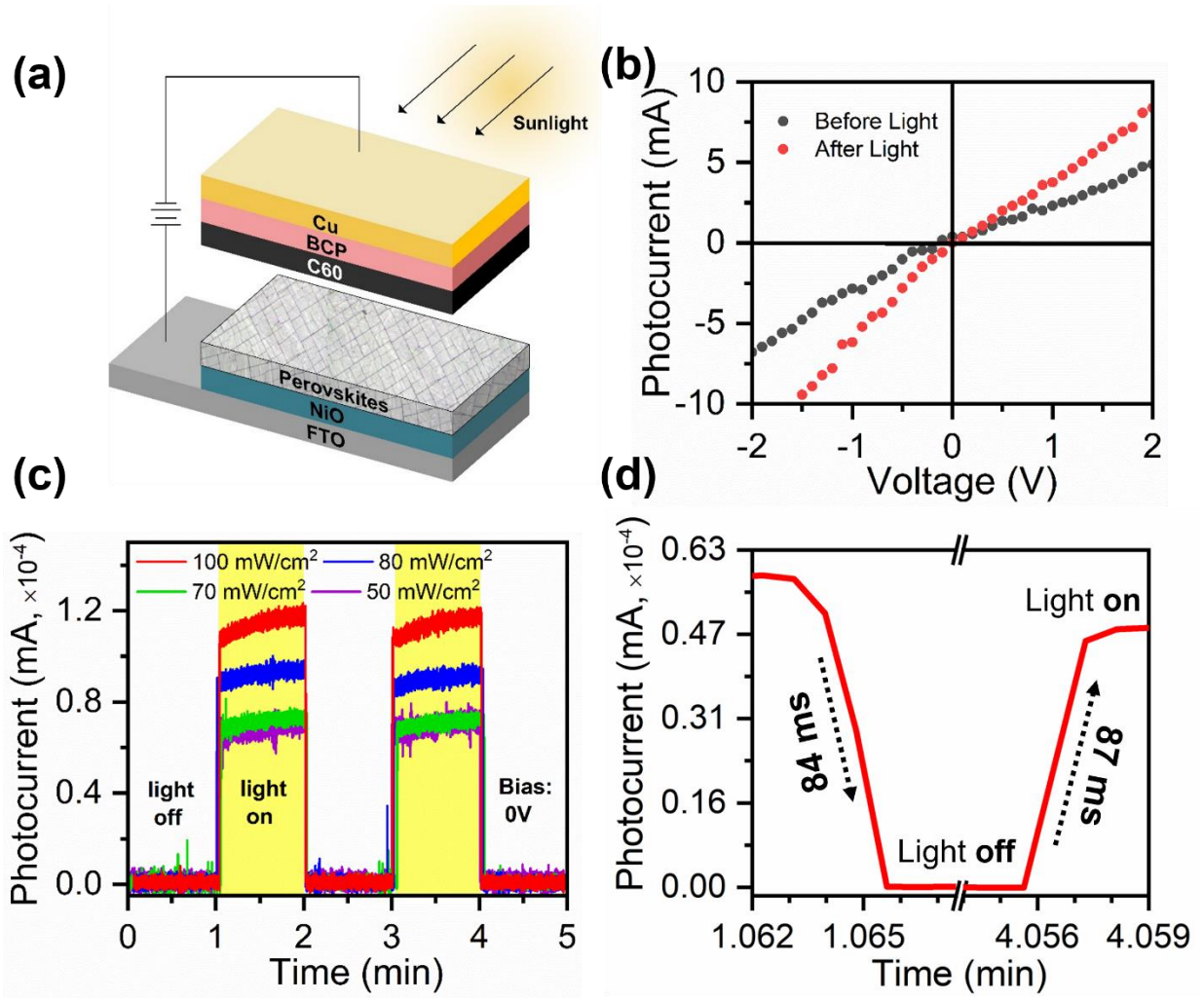

Figure 5. | 2D Perovskites film Photodetector device. (a) Schematic structure for photodetector device based on $Cs_2SnI_2Cl_2$. (b) Photocurrent curve before and after exposure to light (c) *I-t* characteristics as a function of light intensity under bias-free condition (d) Decay and rise time of photodetector device.

Figure 5a shows a schematic of the photodetector structure under sunlight based on Sn-based n=1 films, which consist of FTO/ NiO/ $Cs_2SnI_2Cl_2$/ C_{60}/ 2,9-dimethyl-4,7- diphenyl-1,10-phenanthroline (BCP)/ Copper (Cu). Since the NiO and FTO can withstand high temperature during CVD growth, the uniform NiO film was spin-coated on FTO electrode substrate as the hole transport layer, and large areas of Sn-based 2D perovskite films covered the whole 1 ×1 cm substrate with 61µm average thickness were then grown for 2 hours on top by CVD method. After, C_{60}, BCP and Cu were deposited on top in sequence by thermal evaporation to act as the electron

transport layer, cathode buffer layer and electrode, respectively.[41] *I-V* characteristics was measured under dark and illuminated conditions and the light was incidented from FTO side. The bias voltage was plotted as the linear function in Figure 5b. The device showed a dark current of 4.88 mA at 2 V applied voltage. Under light, we observed the photocurrent increased to 8.39 mA at bias of voltage of 2 V due to incident photonic energy with photo-to-current ratio $(I_{light}-I_{dark})/I_{dark}$ of 0.72. Bias-free intensity dependence *I-T* measurements were performed under various light intensities ranging from 50 to 100 mW/cm^2, and the photocurrent was recorded for a period of 300 s. Obvious photocurrent enhancement was captured and remained stable under different illumination conditions, in Figure 5c, revealing the photodetector's sensitivity, reproducible photocurrents and charge carrier generation. In addition, this device shows a quick response with a decay time of 84 ms and a raise time of 87ms in Figure 5d. These response times surpass most of those observed in Sn-based perovskites incorporating organic cations[42–46] and are comparable to their inorganic cation counterparts,[47–51] indicating fast capacitive states response from the Sn-based n=1 film surface.[31]

Conclusion

In the current study, we have established that chemical vapor deposition (CVD) is an effective and scalable technique for the synthesis of all-inorganic 2D lead and tin-based perovskite films, achievable under atmospheric conditions on a variety of substrates. CVD fabrication of large-area, all-inorganic 2D RP lead-based $Cs_2PbI_2Cl_2$ (n=1) and tin-based $Cs_2SnI_2Cl_2$ (n=1) perovskites at atmospheric pressure, yields millimeter-sized films. Additionally, we experimentally confirm the existence of bilayered 2D inorganic RP phases of $Cs_3Pb_2I_3Cl_4$ (n=2) and $Cs_3Sn_2I_3Cl_4$ (n=2). Using a broad battery of experimental techniques we have shown that the structures prefer to orient with the 2D perovskite layers parallel to the substrates for both Pb and Sn compositions. Optical spectroscopy provides distinct optical band gaps for Pb-based n=1 and n=2, and Sn-based n=1 and n=2. The crystallinity of the CVD-grown films remains consistent with varying growth times. Significantly, our work culminates in the successful fabrication of a lead-free photodetector employing Sn-based films, which demonstrated an enhanced, bias-free, and reproducible photocurrent response with a rapid response time. These findings collectively contribute to the

advancement of scalable fabrication techniques, expanding the scope of practical applications of all inorganic halide perovskites in high-performance optoelectronic devices.

Methods

CVD growth of $Cs_2PbI_2Cl_2$ (n=1) film. The $Cs_2PbI_2Cl_2$ (n=1) films were synthesized in a 1 in. diameter quartz tube under ambient pressure with high purity nitrogen as carrier gas. CsCl powder (250mg, 99.999%, Libra) and PbI_2 powder (400mg, 99.999%, Libra) were mixed and placed in a quartz boat on the upper stream. Clean FTO, c-plane sapphire, SiO2, glass and NiO on FTO with 1×1cm size were used as substrates. Substrates were "face-on" placed on the downstream position, which were 10cm away inside the ending side furnace thermal block. Before heating, 600sccm high flow rate carrier gas was turned on for 30min to purge the tube. After that, the furnace was ramped to 600°C within 20min and kept at 600°C for 15min deposition time with 80sccm carrier gas flow rate. When the growth was terminated, the furnace was opened and cooled down to room temperature with a fast-cooling rate.

CVD growth of $Cs_3Pb_2I_3Cl_4$ (n=2) film. The $Cs_3Pb_2I_3Cl_4$ (n=2) films were synthesized in the same diameter quartz tube under ambient pressure with the same carrier gas. CsCl powder (150mg, 99.999%, Libra), PbI_2 powder (400mg, 99.999%, Libra) and $PbCl_2$ powder (100mg, 99.999%, Libra) were mixed and placed in a quartz boat on the upper stream. Clean FTO, SiO_2, glass and NiO on FTO with 1×1cm size were used as substrates and were "face-on" placed on the downstream position, which were 3cm away inside the ending side furnace thermal block. Heating, carrier gas flowrate, and cooling conditions were the same as Pb n=1.

CVD growth of $Cs_2SnI_2Cl_2$ (n=1) film. The $Cs_2SnI_2Cl_2$ (n=1) films were synthesized in the same diameter quartz tube under ambient pressure with the same carrier gas. CsCl powder (250mg, 99.999%, Libra) and SnI_2 powder (375mg, 99.99%, Sigma) were mixed and placed in a quartz boat on the upper stream. Clean FTO, glass and NiO on FTO with 1×1cm size were used as substrates and were "face-on" placed on the downstream position, which were 7cm away inside the ending side furnace thermal block. During the growth, the furnace was ramped to 650°C within 20min and kept at 650°C for 15min deposition time with 80sccm carrier gas flow rate. Cooling conditions were the same as Pb n=1.

CVD growth of $Cs_3Sn_2I_3Cl_4$ (n=2) film. The $Cs_3Sn_2I_3Cl_4$ (n=2) films were synthesized in the same diameter quartz tube under ambient pressure with the same carrier gas. CsCl powder (100mg, 99.999%, Libra), SnI_2 powder (187.5mg, 99.99%, Sigma) and $SnCl_2$ powder (187.5mg, 99.999%, Libra) were mixed and placed in a quartz boat on the upper

stream. Cleaned FTO, glass and NiO on FTO with 1×1cm size were used as substrates and were "face-on" placed on the downstream position, which were 1cm away inside the ending side furnace thermal block. During the growth, the furnace was ramped to 650°C within 20min and kept at 650°C for 15min deposition time with 80sccm carrier gas flow rate. Cooling conditions were the same as Pb n=1.

Unit cell parameters extraction from powder diffraction patterns. For the Pb-based n=2 compounds: Extraction of Parameter c: The parameter c was determined from the XRD data corresponding to the (00l) planes. Extraction of Parameters a and b: The parameters a and b were obtained from the diffraction patterns of the (101) and (202) planes. For the Sn-based n=2 compounds: Extraction of Parameter c: The parameter c was determined from the XRD data corresponding to the (00l) planes. Extraction of Parameters a and b: The parameters a and b were obtained from the diffraction patterns of the (107) plane.

GIWAXS Measurement and Analysis. Diffraction spectra used in this paper were high-resolution synchrotron GIWAXS patterns measured at National Synchrotron Light Source II (NSLS-II) beamline 11-BM (Complex Materials Scattering beamline). Samples were placed in a vacuumed chamber (10-2 torr) and were 287mm away from a Pilatus 300M area detector. The photon energy was 13.5 keV, and the beam size was 200 μm × 50 μm (Height × Vertical). GIWAXS patterns were processed using SciAnalysis (https://github.com/CFN softbio/SciAnalysis) running on Visual Studio Code using Python (v.3.7.3)

Optical spectroscopy. The optical absorbance of the samples was measured by illuminating the samples with a monochromatic light, which was spectrally selected from a quartz-tungsten-halogen light source through a monochromator (SpectraPro HRS 300, Princeton instruments). The incident light was modulated by a chopper at 2kHz, and synchronous detection of the transmitted light was collected by a silicon photodiode connected to a lock-in amplifier (SR865, Stanford Research Systems). The absorbance data was acquired from 340-775 nm with a dwell time of 0.1s. The optical band gaps were estimated by Tauc plot. All the samples were measured in air under ambient conditions during acquisition. Steady-state and time-resolved photoluminescence (PL) spectra were collected using an Edinburgh Instruments FS5 spectrofluorometer at room temperature with a 375 nm pulsed laser diode excitation source for time-resolved measurements and steady-state spectra collection as well as with a wavelength-tunable 150 W Xe lamp for steady-state spectra acquisition.

Photodetector device fabrication. We used an inverted planar architecture FTO/NiO/perovskite-film/C60/Cu for the fabrication of a self-powered photodetector. First, we prepared the top part of our solar cells consisting of the patterned fluorine doped tin oxide (FTO, Thin Film Device Inc.) substrates and the hole transporting layer (HTL). The FTO substrates were washed in water, acetone, acetone/ethanol (50:50) and isopropyl alcohol by ultrasonication for 15 min, respectively. The substrates were further dried under argon airflow and treated with UV for 30 min. Then, a NiO solution was spin-coated on the clean FTO substrates at 5000 revolutions per minute (r.p.m.) for 30 s (layer thickness was about 30 nm). The NiO solution was prepared by dissolving 0.1 M nickel acetate tetrahydrate and monoethanolamine (1:1) in anhydrous ethanol. The solution was left on the hot plate stirring at 70°C for 3 h. Then the

$Cs_2SnI_2Cl_2$ (n=1) films were CVD grown on NiO coated FTO substrate in a 1 in. diameter quartz tube under ambient pressure with the same carrier gas. CsCl powder (500mg, 99.999%, Libra) and SnI_2 powder (750mg, 99.99%, Sigma) were mixed and placed in a quartz boat on the upper stream, 1×1cm size FTO/NiO substrates were "face-on" placed on the downstream position, which were 7cm away inside the ending side furnace thermal block. During the growth, the furnace was ramped to 650°C within 20min and kept for 120min deposition time with 80sccm carrier gas flow rate. Other growth conditions were the same as Pb n=1.

The FTO/NiO/ $Cs_2SnI_2Cl_2$ (n=1) perovskite was subsequently transferred to an argon-filled glovebox for the rest of the solar cell fabrication process. We further evaporate C60 with a thickness of 30 nm at a rate of 0.1 Å /s. Following this, we evaporated BCP having a thickness of 1 nm with using a thermal evaporator. The solar cell devices were completed by evaporating a 100 nm layer of copper using a shadow mask yielding eight cells of 31.4 mm2 per 1'x1' area of the sample device.

Supporting Information

X-Ray Photoelectron Spectroscopy Characterization, Transmission Electron Microscopy Characterization, Profilometer Characterization, X-Ray Diffraction Characterization, Scanning Electron Microscopy Characterization, Density functional theory calculations, Microscope images under different substrates and temperatures, Comparison of XRD plots, SEM image, TEM and HAADF-STEM images, Stimulated powder diffraction patterns, EDAX and atomic ratio results, Linear fitting of $(\beta(s)/S)^2$ as a function of $\beta(s)/S^2$, Tauc plots, TRPL spectrum, Crystallographic structures, and DFT computed electronic band structures.

Acknowledgements

A.D.M. and X.S. acknowledge research support from the HydroGEN Advanced Water Splitting Materials Consortium, established as part of the Energy Materials Network under the U.S. Department of Energy, Office of Energy Efficiency and Renewable Energy, Hydrogen and Fuel Cell Technologies Office, under the Award Number DE-EE0008843. J.H. acknowledges the financial support from the China Scholarships Council (No. 202107990007). The work at ISCR and FOTON was supported by the European Union's Horizon 2020 research and innovation program under grant agreement 861985 (PeroCUBE). J.E. acknowledges the financial support from the Institut Universitaire de France. This work was granted access to the HPC resources of TGCC/CINES under the allocation A0140911434 made by GENCI. At Northwestern, this work was supported by the Office of Naval Research (ONR) under grant N00014-20-1-2725. The authors acknowledge the support from Esther Tsai for her assistance in performing GIWAXS measurements at the beamline, BNL.

References

1. Blancon, J. C. *et al.* Scaling law for excitons in 2D perovskite quantum wells. *Nat. Commun.* **9**, 1–10 (2018).

2. Blancon, J. C. *et al.* Extremely efficient internal exciton dissociation through edge states in layered 2D perovskites. *Science (80-.).* **355**, 1288–1292 (2017).

3. Tsai, H. *et al.* Stable Light-Emitting Diodes Using Phase-Pure Ruddlesden–Popper Layered Perovskites. *Adv. Mater.* **30**, (2018).

4. Zhang, Y. & Park, N. Quasi-Two-Dimensional Perovskite Solar Cells with E ffi ciency Exceeding 22%. (2022) doi:10.1021/acsenergylett.1c02645.

5. Li, J. *et al.* Air-Stable Direct Bandgap Perovskite Semiconductors: All-Inorganic Tin-Based Heteroleptic Halides AxSnClyIz (A = Cs, Rb). *Chem. Mater.* **30**, 4847–4856 (2018).

6. Xu, Z., Chen, M. & Liu, S. F. Layer-Dependent Ultrahigh-Mobility Transport Properties in All-Inorganic Two-Dimensional Cs2PbI2Cl2 and Cs2SnI2Cl2 Perovskites. *J. Phys. Chem. C* (2019) doi:10.1021/acs.jpcc.9b09512.

7. Li, J. *et al.* Cs2PbI2Cl2, All-Inorganic Two-Dimensional Ruddlesden-Popper Mixed Halide Perovskite with Optoelectronic Response. *J. Am. Chem. Soc.* **140**, 11085–11090 (2018).

8. Guo, S. *et al.* Enhanced Photocurrent of All-Inorganic Two-Dimensional Perovskite Cs2PbI2Cl2via Pressure-Regulated Excitonic Features. *J. Am. Chem. Soc.* **143**, 2545–2551 (2021).

9. Acharyya, P. *et al.* Intrinsically Ultralow Thermal Conductivity in Ruddlesden-Popper 2D Perovskite Cs2PbI2Cl2: Localized Anharmonic Vibrations and Dynamic Octahedral Distortions. *J. Am. Chem. Soc.* **142**, 15595–15603 (2020).

10. Yang, S. *et al.* 2D Cs2PbI2Cl2 Nanosheets for Holistic Passivation of Inorganic CsPbI2Br Perovskite Solar Cells for Improved Efficiency and Stability. *Adv. Energy Mater.* **10**, 1–10 (2020).

11. Acharyya, P., Maji, K., Kundu, K. & Biswas, K. 2D Nanoplates and Scaled-Up Bulk Polycrystals of Ruddlesden-Popper Cs2PbI2Cl2 for Optoelectronic Applications. *ACS Appl. Nano Mater.* **3**, 877–886 (2020).

12. Zhan, Y., Liu, Z., Najmaei, S., Ajayan, P. M. & Lou, J. Large-area vapor-phase growth and characterization of MoS 2 atomic layers on a SiO 2 substrate. *Small* **8**, 966–971 (2012).

13. Li, T. *et al.* Epitaxial growth of wafer-scale molybdenum disulfide semiconductor single

crystals on sapphire. *Nat. Nanotechnol.* **16**, 1201–1207 (2021).

14. Liu, Z. *et al.* Direct growth of graphene/hexagonal boron nitride stacked layers. *Nano Lett.* **11**, 2032–2037 (2011).

15. Roy, S. *et al.* Structure, Properties and Applications of Two-Dimensional Hexagonal Boron Nitride. *Adv. Mater.* **33**, 1–48 (2021).

16. Zhou, Y. *et al.* Millimeter-Size All-inorganic Perovskite Crystalline Thin Film Grown by Chemical Vapor Deposition. *Adv. Funct. Mater.* **31**, 1–11 (2021).

17. Chen, J. *et al.* Vapor-Phase Epitaxial Growth of Aligned Nanowire Networks of Cesium Lead Halide Perovskites (CsPbX3, X = Cl, Br, I). *Nano Lett.* **17**, 460–466 (2020).

18. Oksenberg, E. *et al.* Large lattice distortions and size-dependent bandgap modulation in epitaxial halide perovskite nanowires. *Nat. Commun.* (2020) doi:10.1038/s41467-020-14365-2.

19. Soto-Montero, T. *et al.* Single-Source Vapor-Deposition of MA1–xFAxPbI3 Perovskite Absorbers for Solar Cells. *Adv. Funct. Mater.* 2300588 (2023) doi:10.1002/ADFM.202300588.

20. Paliwal, A., Zanoni, K. P. S., Roldá N-Carmona, C., Angeles Herná Ndez-Fenollosa, M. & Bolink, H. J. Fully vacuum-deposited perovskite solar cells in substrate configuration. *Matter* (2023) doi:10.1016/j.matt.2023.07.011.

21. Vacuum deposition of CsPbI 3 layers on textured Si for Perovskite/Si tandem solar cells. (2019) doi:10.7567/1347-4065/aafb56.

22. Sahli, F. & Werner, J. Fully textured monolithic perovskite/silicon tandem solar cells with 25.2% power conversion efficiency. doi:10.1038/s41563-018-0115-4.

23. Haider, M. I. *et al.* Ethylenediamine Vapors-Assisted Surface Passivation of Perovskite Films for Efficient Inverted Solar Cells. *Sol. RRL* **7**, 2201092 (2023).

24. Malekshahi Byranvand, M. *et al.* Chemical vapor deposited polymer layer for efficient passivation of planar perovskite solar cells. *J. Mater. Chem. A* **8**, 20122–20132 (2020).

25. Chen, H. *et al.* Multistep nucleation and growth mechanisms of organic crystals from amorphous solid states. *Nat. Commun.* **10**, 1–10 (2019).

26. Abzieher, T. *et al.* From Groundwork to Efficient Solar Cells: On the Importance of the Substrate Material in Co-Evaporated Perovskite Solar Cells. *Adv. Funct. Mater.* **31**, (2021).

27. Yang, Y. *et al.* Suppressing Vacancy Defects and Grain Boundaries via Ostwald Ripening for High-Performance and Stable Perovskite Solar Cells. *Adv. Mater.* **32**, 1–7 (2020).

28. Lanzetta, L., Aristidou, N. & Haque, S. A. Stability of Lead and Tin Halide Perovskites: The Link between Defects and Degradation. *J. Phys. Chem. Lett.* **11**, 574–585 (2020).

29. Ruddlesden, S. N. & Popper, P. New compounds of the K 2 NIF 4 type . *Acta Crystallogr.* **10**, 538–539 (1957).

30. Stoumpos, C. C. *et al.* Ruddlesden-Popper Hybrid Lead Iodide Perovskite 2D Homologous Semiconductors. *Chem. Mater.* **28**, 2852–2867 (2016).

31. Ramasamy, P. *et al.* All-inorganic cesium lead halide perovskite nanocrystals for photodetector applications. *Chem. Commun.* **52**, 2067–2070 (2016).

32. 名古屋工業大学学術機関リポジトリ. https://nitech.repo.nii.ac.jp/records/2389.

33. Tsai, H. *et al.* Light-induced lattice expansion leads to high-efficiency perovskite solar cells. *Science (80-.).* **360**, 67–70 (2018).

34. Sen, S. K. *et al.* X-ray peak profile analysis of pure and Dy-doped α-MoO3 nanobelts using Debye-Scherrer, Williamson-Hall and Halder-Wagner methods. *Adv. Nat. Sci. Nanosci. Nanotechnol.* **11**, 025004 (2020).

35. Kinigstein, E. D. *et al.* Edge States Drive Exciton Dissociation in Ruddlesden-Popper Lead Halide Perovskite Thin Films. *ACS Mater. Lett.* **2**, 1360–1367 (2020).

36. Waleed, A. *et al.* All inorganic cesium lead iodide perovskite nanowires with stabilized cubic phase at room temperature and nanowire array-based photodetectors. *Nano Lett.* **17**, 4951–4957 (2017).

37. Hsu, H. C., Wu, Z. Y., Chen, Y. Y. & Lin, L. J. Room-temperature near-infrared random lasing with tin-based perovskites prepared by cvd processing. *J. Phys. Chem. C* **125**, 5180–5184 (2021).

38. Jiang, Y., Wei, J. & Yuan, M. Energy-Funneling Process in Quasi-2D Perovskite Light-Emitting Diodes. *J. Phys. Chem. Lett.* **12**, 2593–2606 (2021).

39. Zhao, S. & Xiao, L. Ion migration mechanism in all-inorganic Ruddlesden–Popper lead halide perovskites by first-principles calculations. *Phys. Chem. Chem. Phys.* **24**, 403–410 (2021).

40. Wang, Z., Wang, Y., Nie, Z., Ren, Y. & Zeng, H. Laser induced ion migration in all-inorganic mixed halide perovskite micro-platelets. *Nanoscale Adv.* **1**, 4459–4465 (2019).

41. Vuong, V. H. *et al.* Engineering Chemical Vapor Deposition for Lead-Free Perovskite-Inspired MA3Bi2I9 Self-Powered Photodetectors with High Performance and Stability. *Adv. Opt. Mater.* **9**, 1–10 (2021).

42. Liu, C.-K. *et al.* Sn-Based Perovskite for Highly Sensitive Photodetectors. *Adv. Sci.* **6**, 1900751 (2019).

43. Waleed, A. *et al.* Lead-Free Perovskite Nanowire Array Photodetectors with Drastically Improved Stability in Nanoengineering Templates. *Nano Lett.* **17**, 523–530 (2017).

44. He, M. *et al.* Sn-Based Self-Powered Ultrafast Perovskite Photodetectors with Highly Crystalline Order for Flexible Imaging Applications. *Adv. Funct. Mater.* **33**, (2023).

45. Yang, Y. *et al.* Sn-based quasi-two-dimensional organic-inorganic hybrid halide perovskite for high-performance photodetectors. *Appl. Phys. Lett.* **119**, 161106 (2021).

46. Qian, L. *et al.* A lead-free two-dimensional perovskite for a high-performance flexible

photoconductor and a light-stimulated synaptic device. *Nanoscale* **10**, 6837–6843 (2018).

47. Cao, F., Tian, W., Wang, M., Wang, M. & Li, L. Stability enhancement of lead-free CsSnI3 perovskite photodetector with reductive ascorbic acid additive. *InfoMat* **2**, 577–584 (2020).

48. Tang, X. *et al.* All-Inorganic Halide Perovskite Alloy Nanowire Network Photodetectors with High Performance. *ACS Appl. Mater. Interfaces* **12**, 4843–4848 (2020).

49. Ma, X. *et al.* A Flexible Plasmonic-Membrane-Enhanced Broadband Tin-Based Perovskite Photodetector. *Nano Lett.* **21**, 9195–9202 (2021).

50. Han, X. *et al.* Lead-Free Double Perovskite Cs2SnX6: Facile Solution Synthesis and Excellent Stability. *Small* **15**, 1901650 (2019).

51. Zhou, J. *et al.* Lead-Free Perovskite Derivative Cs2SnCl6−xBrx Single Crystals for Narrowband Photodetectors. *Adv. Opt. Mater.* **7**, 1900139 (2019).

For Table of Contents Only